RSC Advances

PAPER

View Article Online
View Journal | View Issue

Cite this: *RSC Adv.*, 2023, **13**, 15190

Ultralight elastic Al_2O_3 nanorod-graphene aerogel for pressure sensing and thermal superinsulation†

Fengqi Liu, Yonggang Jiang, * Junzong Feng, Liangjun Li and Jian Feng *

Received 16th February 2023
Accepted 24th April 2023

DOI: 10.1039/d3ra01070h

rsc.li/rsc-advances

Novel nanorod aerogels have gained tremendous attention owing to their unique structure. However, the intrinsic brittleness of ceramics still severely limits their further functionalization and application. Here, based on the self-assembly between one-dimensional (1D) Al_2O_3 nanorods and two-dimensional (2D) graphene sheets, lamellar binary Al_2O_3 nanorod-graphene aerogels (ANGAs) were prepared by the bidirectional freeze-drying technique. Thanks to the synergistic effect of rigid Al_2O_3 nanorods and high specific extinction coefficient elastic graphene, the ANGAs not only exhibit robust structure and variable resistance under pressure, but also possess superior thermal insulation properties compared to pure Al_2O_3 nanorod aerogels. Therefore, a series of fascinating features such as ultra-low density (3.13–8.26 mg cm^{-3}), enhanced compressive strength (6 times higher than graphene aerogel), excellent pressure sensing durability (500 cycles at 40% strain) and ultra-low thermal conductivity (0.0196 W m^{-1} K^{-1} at 25 °C and 0.0702 W m^{-1} K^{-1} at 1000 °C) are integrated in ANGAs. The present work provides fresh insight into the fabrication of ultralight thermal superinsulating aerogels and the functionalization of ceramic aerogels.

1. Introduction

Among the wide range of aerogels, ceramic aerogels distinguish themselves by their low density, high porosity and excellent heat resistance, and demonstrate great potential for applications in the fields of thermal insulation, catalysis, adsorption, *etc.*[1–3] However, their further practical applications are severely limited by their intrinsic brittleness due to the point-to-point contact between the particle building units. The addition of strengthening phases, such as fibers,[4,5] whiskers[6,7] or polymers,[8,9] can improve the mechanical properties of ceramic aerogels, but brings a significant increase in density (over 0.2 g cm^{-3}), and the addition of polymers sacrifices the temperature resistance of ceramic aerogels. To overcome these problems, flexible ceramic fibers are used as basic assembly units for building fiber aerogels with excellent elasticity.[10–12] However, the thermal conductivity of the fiber aerogel increases significantly at high temperatures because the macroporous structure of the fibrous skeleton is not conducive to suppressing the radiative heat transfer at elevated temperatures.[13,14]

Different from nanoparticle or nanofiber microstructures, the emerging nanorod aerogels stand out with its unique structure and excellent properties.[15] Nanorods with high aspect ratio not only can form a continuous microstructure instead of inefficient connections between particles, but also can introduce nanoscale pores that facilitate thermal insulation. So far, there are few reports on novel nanorod aerogels, and the only reports are focused on Al_2O_3 nanorod aerogels (ANAs). Zhang *et al.*[16] prepared low-density (0.146 g cm^{-3}) Si-doped Al_2O_3 nanorod aerogels with a compressive strength of 1.50 MPa and a thermal conductivity of 0.089 W m^{-1} K^{-1} at 1200 °C. Our previous work developed carbon-coated Al_2O_3 nanorod aerogels with densities as low as 0.086 g cm^{-3}, which exhibited enhanced compressive strength (2.98 MPa) and thermal insulation properties (0.065 W m^{-1} K^{-1} at 1200 °C).[15] However, the intrinsic brittleness of the Al_2O_3 nanorod aerogels were not fundamentally improved by either the fiber-reinforced or the carbon-coated strategy,[17] and brittle fracture still occurred at large strains, which is not favorable for thermal insulation applications in structures with variable dimensions. Therefore, the fabrication of elastic Al_2O_3 nanorod aerogels remains a great challenge.

Graphene, as an advanced 2D material with high mechanical strength, large specific surface area and excellent electrical conductivity, is considered an attractive candidate for the construction of multifunctional three-dimensional (3D) aerogels.[18,19] Although graphene has high thermal conductivity within layers,[20] directionally aligned graphene sheet layers can effectively block the heat transfer between layers and thus obtained graphene aerogels (GAs) can exhibit low thermal conductivity.[21] In addition, graphene, which has excellent electrical conductivity, is also an ideal material for sensor applications.[22] Nevertheless, pure graphene aerogels generally exhibit poor mechanical properties and severe volume shrinkage due to the weak van der Waals interactions between

Science and Technology on Advanced Ceramic Fibers and Composites Laboratory, College of Aerospace Science and Technology, National University of Defense Technology, Changsha 410073, P. R. China. E-mail: jygemail@nudt.edu.cn; fengj@nudt.edu.cn

† Electronic supplementary information (ESI) available. See DOI: https://doi.org/10.1039/d3ra01070h

the building blocks,[23] so components such as carbon nanotubes,[24] polymers[25] and ceramics[26] are incorporated to enhance the graphene backbone strength and promote efficient load transfer. The reinforced graphene aerogels then can acquire excellent mechanical properties with reasonable structural design, such as chemical vapor deposition (CVD),[27] directional freezing[28] and 3D printing.[29] However, although the carbon nanotube-modified graphene aerogels feature high elasticity, the maximum compressive stretch and elastic modulus are not significantly improved due to the softness of the carbon skeleton, which results in a significant reduction in the detection range of pressure sensing. Hybridization of polymers with graphene can impart enhanced elasticity and compressive strength to the aerogels, but the obtained hybrid aerogels are difficult to apply for high temperature insulation due to the mismatch of heat resistance.[30]

In recent years, high temperature resistant ceramic component has been used to composite with graphene to obtain robust aerogels. Zhang *et al.*[31] constructed hybrid aerogels with high compressive and strong mechanical properties by depositing Al_2O_3 nanolayers on graphene backbone, which can achieve strains up to 80% and a three-fold increase in maximum compressive strength compared to pure graphene aerogels. However, the high cost and relatively low efficiency of the atomic layer deposition (ALD) method limit its mass production. Xu *et al.*[32] developed a versatile method for building elastic aerogels by combining graphene with ceramic fibers, but as mentioned above, the micron-sized holes introduced by the fibers have negative effects on the thermal insulation properties of the aerogels. Additionally, Yin *et al.*[33] also attempted to mechanically incorporate oxide particles (TiO_2, CeO_2 and Fe_2O_3) into graphene, but the inevitable aggregation of particles leads to defect generation and performance degradation. Hence, new types of ceramic additives need to be investigated for the simple preparation of elastic ceramic-graphene aerogels for high temperature thermal insulation and pressure sensing.

Here, laminated binary Al_2O_3 nanorods-graphene aerogels (ANGAs) based on intermolecular interactions and bidirectional freeze-drying techniques were successfully prepared. The advantageous complementary effect between rigid Al_2O_3 nanorods and flexible graphene sheets confers the desired properties to ANGAs. As reinforcing phase, Al_2O_3 nanorods were tightly adsorbed onto graphene sheets by hydrogen bonding, resulting in substantially elevated compressive strength of ANGAs compared to graphene aerogels (GAs). The flexible graphene sheets are interconnected to form a robust elastic conductive backbone, which overcomes the brittleness of Al_2O_3 ceramics and enables ANGAs to exhibit excellent pressure sensing properties. More importantly, the graphene sheets with high specific extinction coefficient not only confine the motion of gas molecules within the layer gap, but also suppress the radiative heat transfer at high temperatures. Consequently, the obtained ANGAs exhibit thermal superinsulation properties over the full temperature range from low to high temperatures. The successful synthesis of ANGAs provides a new strategy for the preparation of multifunctional elastic ceramic-based aerogels.

2. Experiments and methods

2.1. Materials

Al_2O_3 nanorods were prepared based on previous work with a diameter of about 10–20 nm and a length of 500–1000 nm.[15] Graphene oxide (GO) dispersion (10–50 μm in diameter) with a concentration of 5 mg mL^{-1} was purchased from Suzhou Tanfeng Graphene Technology Co., Ltd. Polyvinyl alcohol (PVA) (98–99% alcohol solubility, $M_w = 5\,000\,000$) were obtained from Macklin Co., Ltd. 184 Silicone Elastomer (PDMS) were bought from Dow Corning Co., Ltd. The ultrapure water machine in laboratory provided deionized water.

2.2. Preparation of ANGAs, GAs and ANAs

A wedge-shaped PDMS with an angle of 30° was combined with a copper rod whose bottom was placed in liquid nitrogen to form a bidirectional freezing platform. A homogeneous mixture of 5 mL of graphene dispersion, 5 mL of PVA solution (0.1 wt%) and a certain amount of Al_2O_3 nanorod sols was obtained after stirring at 500 rpm for 1 h. The beaker with the mixed solution was placed on the bidirectional freezing platform, and the Al_2O_3 nanorod-graphene aerogels (ANGAs) were obtained after 48 h freeze-drying process and 2 h treatment in argon atmosphere at 800 °C. The mass ratio of Al_2O_3 sols to the mixed solution (graphene dispersion and PVA solution) was determined as the Al_2O_3 content, and the samples with 2%, 4%, 6%, 8% and 10% Al_2O_3 content were named as ANGA-2, ANGA-4, ANGA-6, ANGA-8 and ANGA-10, respectively. The graphene aerogels (GAs) were prepared by the same procedure as ANGAs, except that Al_2O_3 nanorod sols are not added. Pure Al_2O_3 nanorod aerogels (ANAs) were prepared based on sample ANGA-10, except that the graphene dispersion was replaced by an equal amount of water.

2.3. Construction and characterization of pressure sensors based on ANGAs

All pressure sensing tests were based on sample ANGA-8. Two copper sheets with dimensions of 5 × 5 × 0.1 cm are connected to the resistance meter (B35, Owon) through two wires, respectively. ANGAs of size 3 × 3 × 3 cm are placed between the copper sheets. The copper sheets were attached to the probe of the mechanical testing machine for programmed control of the strain of the sample with a loading/unloading speed of 20 mm min^{-1}. The resistance of the sample in the initial state (0% strain) is defined as R_0, and the resistance of the sample after compression is defined as R_t. The change in resistance (ΔR) is the difference between R_0 and R_t. $\Delta R/R_0$ is defined as the sensor response. We define the sensor response fluctuation as:

$$R_f = \frac{R_{max} - R_{min}}{R_{ave}} \times 100\%$$

where R_f is the response fluctuation (%), R_{max} is the maximum value of sensor response, R_{min} is the is the minimum value of sensor response, and R_{ave} is the is the average value of sensor response.

2.4. Characterization

A ZEISS scanning electron microscope (Sigma 300, Germany) was applied to obtain SEM images and EDS mappings. XRD spectra were recorded with an alpha diffractometer (Panalytical, The Netherlands) at Cu-Kα radiation (40 kV, 40 mA). FL4204GL universal testing machine (Fuller Test Technology) was used to evaluate the mechanical properties of the samples at a motion rate of 1 mm min^{-1}. Thermogravimetric-differential scanning calorimetry (TG-DTA) was tested by a NETZSCH thermogravimetric analyzer (STA 449F3, Germany) (argon flow rate of 50 mL min^{-1} and heating rate of 10 °C min^{-1}). Sample surface temperature changes were monitored by a M200A infrared camera (InfiRay). The room temperature thermal conductivity (air atmosphere) in the direction perpendicular to the laminate structure was tested by Hotdisk (TPS2000s, Switzerland). The high temperature thermal conductivity (argon atmosphere) of the sample was measured in an argon atmosphere by TPS2000s. Non-covalent interactions between graphene and Al_2O_3 nanorods were simulated by density functional theory (DFT) through the CP2K quantum chemistry package.

3. Results and discussion

3.1. Fabrication and characterization of ANGAs

In order to obtain ANGAs with excellent thermal insulation and pressure sensing properties, the following principles need to be taken into account: (i) establishing interactions between the Al_2O_3 nanorods and the graphene sheets so that the two can be uniformly and tightly bounded, rather than unevenly dispersed by mechanical mixing; (ii) forming stable chemical crosslinks between graphene sheets for building a robust elastic backbone; (iii) orienting the graphene sheets to minimize layer-to-layer heat transfer, thus reducing the thermal conductivity.

The preparation process of ANGAs is shown in Fig. 1a. After homogeneous dispersion of Al_2O_3 nanorods and graphene in polyvinyl alcohol (PVA) solution, elastic ANGAs with layer-like structure were obtained after bi-directional freezing, vacuum drying and high temperature annealing. By adjusting the content of Al_2O_3 nanorods, ultralight ANGAs with low densities ranging from 3.13–8.26 mg cm^{-3} could be obtained, which can be evidenced by samples standing stably on top of a brush (Fig. 2a). Benefiting from the abundant hydroxyl groups on the surface of Al_2O_3 nanorods as well as graphene oxide (GO), strong hydrogen bondings can be formed between the two, which is proved by the calculation of non-covalent bonded intermolecular interactions (Fig. 2b). The shifts of the C=O and Al–O peaks in the FTIR spectra after the combination of Al_2O_3 nanorods and GO also indicate the formation of hydrogen bondings (Fig. S1†). In addition, as shown in the mapping image (Fig. 2c), the C, Al and O elements are homogeneously dispersed on the graphene sheets. This is because the Al_2O_3 can be trapped by the target sites (–OH) on the graphene surface under the induction of hydrogen bonding, and then uniformly distributed on the graphene sheet surface to self-assemble into nanoceramic-enhanced graphene heterostructures. While PVA acts as a chemical cross-linking agent to firmly weld the graphene structural units together after annealing, thus forming a stable skeleton.[34,35] To obtain the desired anisotropic graphene structure, the bidirectional freezing technique was employed for the preparation of ANGAs. The temperature gradient from the bidirectional freezing platform in two directions makes the ice crystals grow in a lamellar pattern and the graphene sheets adsorbed with Al_2O_3 nanorods are extruded

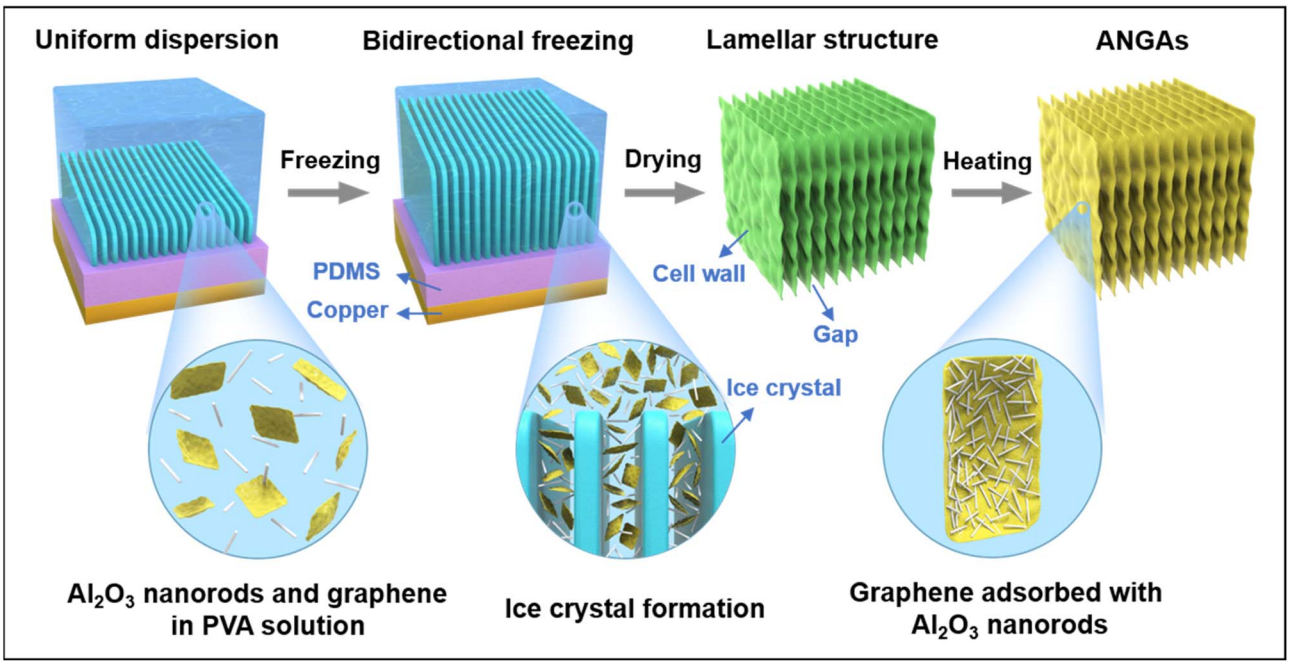

Fig. 1 Schematic diagram of the preparation process of ANGAs.

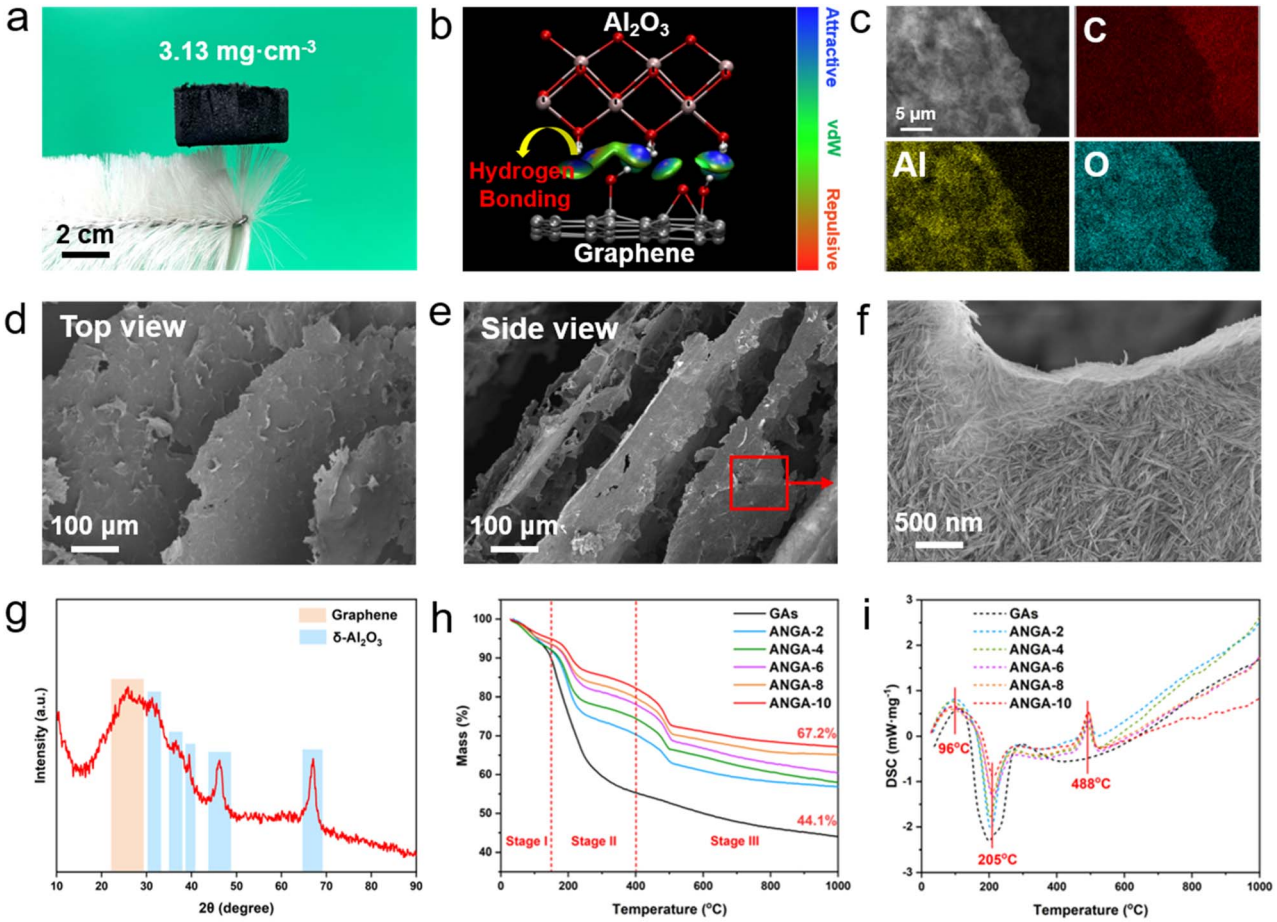

Fig. 2 (a) Photograph of ultralight ANGAs standing on a brush. (b) Non-covalent interaction analysis between Al_2O_3 nanorods and graphene. (c) EDS mapping images of the distribution of C, O and Al elements in ANGAs. SEM images of ANGAs in (d) top view and (e) side view. (f) SEM image of ANGAs showing the Al_2O_3 nanorod-graphene composite structure. (g) XRD patterns of ANGAs. (h) TG curves and (i) DSC curves of GAs and ANGAs with different Al_2O_3 nanorod contents.

into the ice crystal interstices. As shown in Fig. 2d and e, the directionally aligned lamellar ANGAs were successfully prepared after the sublimation of the ice crystals and annealing. As can be seen in enlarged SEM image (Fig. 2f), the rigid Al_2O_3 nanorods, similar to steel rebars in cement, serve as reinforcement for the graphene nanosheets at the nanoscale, which provides a structural basis for the enhanced compressive strength of ANGAs. The enlarged SEM, TEM images and EDS mappings of the ANGAs also indicate that the submicron Al_2O_3 nanorods are closely attached to the large-size graphene sheets, and the distribution of Al and C elements further proves the composition of the ANGAs (Fig. S2–S4†).

The crystalline phase composition of ANGAs was also explored by XRD. As seen in Fig. 2g, nanorods are composed of δ-Al_2O_3, which is transformed from the original boehmite phase after heat treatment,[36] and graphene was evidenced by the broad peak at around 25°. The thermal decomposition processes of ANGAs with different Al_2O_3 nanorod contents and graphene aerogels (GAs) during calcination were further analyzed by TG-DSC (Fig. 2h and i). At temperatures below 150 °C (Stage I), the weight loss of the samples was mainly caused by the removal of adsorbed moisture, which was proved by the exothermic peak at 96 °C in the DSC curves. In Stage II (150–400 °C), the significant weight loss is mainly attributed to the pyrolysis of oxygen-containing functional groups in graphene (–OH, –COOH, –COC–) and the production of CO, CO_2 and water, *etc.*[37] The TG-DSC curves of ANGAs and GAs in Stage III (above 400 °C) are distinctly different. For GAs, the removal of the more stable functional groups and the decomposition of organic carbon leads to the weight loss in Stage III.[38] In contrast, for ANGAs, a significant exothermic peak was observed at 488 °C due to the crystalline phase transition of Al_2O_3 nanorods from boehmite to γ-Al_2O_3.[36] Notably, thanks to the excellent heat resistance of Al_2O_3, the sample residue increased remarkably with the increase of Al_2O_3 nanorods content from 44.1% for GAs to 67.2% for ANGA-10, indicating that the addition of Al_2O_3 nanorods could significantly improve the thermal stability of the aerogels.

3.2. Mechanical properties of ANGAs

Ceramics are known to be intrinsically brittle and the previously reported Al_2O_3 nanorod aerogels are also subject to structural collapse under large deformation.[15,16] However, the situation changes for ANGAs, where the rigid Al_2O_3 nanorods exhibit

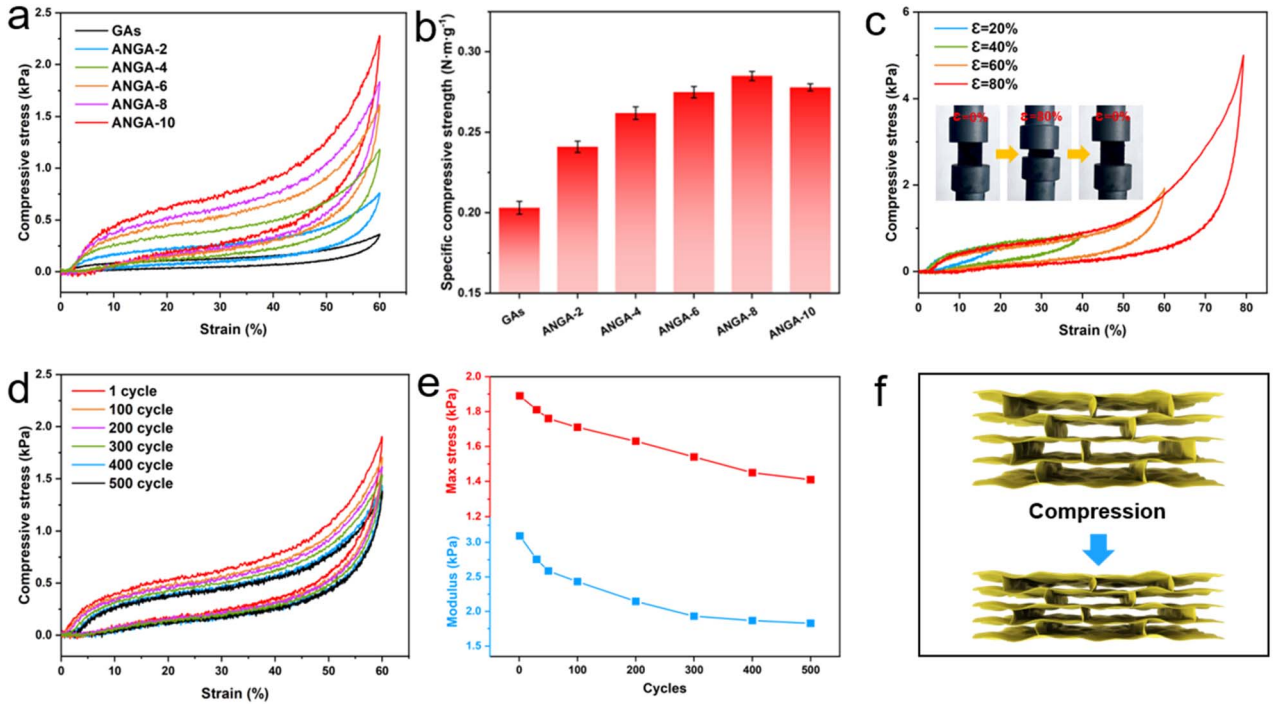

Fig. 3 (a) Stress–strain curves (60% strain) and (b) corresponding specific compressive strength of GAs and ANGAs with different Al_2O_3 nanorod contents. (c) Stress–strain curves and compression process (inset) of ANGA-8 at different strains (20–80% strain). (d) Stress–strain curves and (e) variation curves of maximum stress and elastic modulus of ANGA-8 after 500 compression cycles (60% strain). (f) Schematic diagram of the structural evolution of ANGAs under pressure.

excellent elasticity after bonding with the graphene backbone and the mechanical properties of graphene are further enhanced by Al_2O_3 nanorods. The compression process of ANGAs undergoes three typical stages, including the elastic deformation stage (less than 10% strain), the plateau stage (10–40% strain) and the densification stage (over than 40% strain). It can be seen from the stress–strain curves of GAs and ANGAs that the compressive strength of the samples at 60% strain increases rapidly by more than 6 times with the increase of Al_2O_3 nanorods content, from 0.36 kPa for GAs to 2.29 kPa for ANGAs-10 (Fig. 3a). Since the increase in Al_2O_3 content also brings about an increase in density, the specific compressive strength is employed to reasonably evaluate the variation in compressive performance. As can be seen from Fig. 3b, the specific compressive strength of the samples increased by more than 40% from 0.203 N m g^{-1} for GAs to 0.286 N m g^{-1} for ANGA-8. With the further increase in Al_2O_3 nanorods, the specific compression strength of the sample decreased (0.278 N m g^{-1} for ANGA-10), so the compression performance of ANGA-8 was further investigated.

Thanks to the interplay of Al_2O_3 nanorods and graphene, ANGA-8 was able to recover to its initial state even at a large strain of 80% and had a compressive strength of 4.98 kPa at 80% strain (Fig. 3c), indicating that it could remain elastic under a pressure of 40 000 times of its own weight. In addition, ANGA-8 demonstrates outstanding compression durability, with only 2.8% plastic deformation after 500 compression cycles (60% strain) (Fig. 3d). Meanwhile, the maximum compression strength decreased from 1.89 kPa to 1.41 kPa, accompanied by a drop in elastic modulus from 3.10 kPa to 1.83 kPa (Fig. 3e). The excellent elasticity of ANGAs and the greatly elevated compressive strength are mainly attributed to the synergistic effect of Al_2O_3 nanorods and graphene framework. Compared with the random structure, the ordered lamellar structure obtained by bidirectional freezing facilitates the formation of more effective force support points. At the macroscopic scale, the elastic bridging layers between the lamellae are able to transfer and dissipate the load efficiently through folding and bending after the graphene skeleton is subjected to pressure (Fig. 3f). At the nanoscale, the rigid Al_2O_3 nanorods act as reinforcing agents and tightly attach to the flexible graphene sheets through intermolecular interactions. The rigid nanorods can support and resist deformation when the graphene sheet is deformed, thus enhancing the compressive strength. In addition, Al_2O_3 nanorod-reinforced graphene units are able to constitute a robust 3D network structure under the bonding effect of PVA. Thus, the 1D nanorods and 2D graphene combine rigidity and flexibility, leading to the birth of ANGAs with excellent mechanical properties.

3.3. Pressure sensing properties of ANGAs

Graphene aerogels are considered to be promising pressure sensors due to their excellent electrical conductivity and elasticity, but pure graphene has a limited pressure detection range due to its low compressive strength and proneness to deformation, which seriously hinders its application. Here, ANGAs not only inherit the properties of graphene aerogels, such as electrical conductivity and elasticity, but also feature enhanced

compressive strength, and thus can effectively extend the upper limit of pressure detection. The conductive network formed by interconnecting Al_2O_3 nanorod-graphene structural units experiences a change in resistance under pressure, as evidenced by changes in the brightness of the light bulb (Fig. 4a and b), together with a robust elastic backbone, providing a structural basis for pressure sensing.

As shown in Fig. 4c, ANGAs are placed between two copper sheets connected with wires to form the pressure sensor. The strains of the ANGAs are precisely controlled by a programmable mechanical tester, and the resistance of the ANGAs is measured by a resistance meter. During the loading process, the porosity of the ANGAs decreases and the lamellar pore walls are moved closer to each other, which is more conducive to rapid electron transfer in the aerogel network, thus exhibiting a lower resistance. After unloading, the resistance returns to the initial state. As shown in Fig. 4d, each compression cycle curve is symmetrical, suggesting that the resistance can recover quickly during

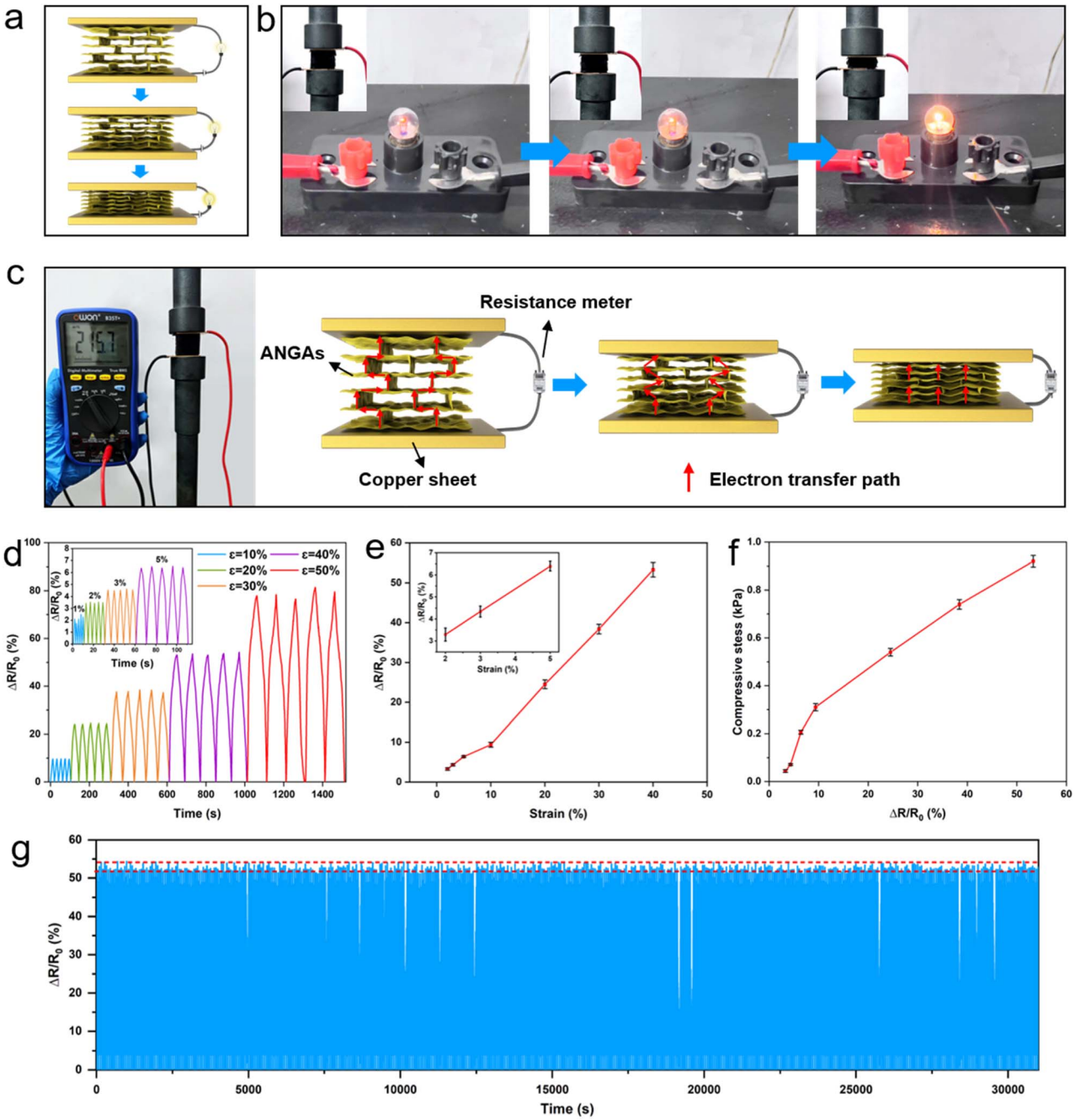

Fig. 4 (a) Schematic diagram and (b) experimental photographs of the change in lamp brightness due to the variation in resistance of ANGAs during compression. (c) Photographs, structure and sensing mechanism of pressure sensor. (d and e) Sensor response curves of the pressure sensor under different strains and (f) the corresponding detection pressure. (g) Sensor response curves of ANGAs under 500 compression cycles at 40% strain.

unloading as well. It can be found that the response stability of ANGAs at 1% strain is poor, with a response fluctuation of 34.29%. Compared with pure GAs, the ANGAs with the addition of non-conductive Al_2O_3 nanorod have higher resistance, which causes the samples to be less sensitive to minor resistance changes caused by small strains. As the strain continued to increase, the stability of the sensor response increased and the response fluctuations decreased to 3.41% for 2% strain, 3.07% for 3% strain, and 2.46% for 5% strain. Also, the response fluctuations at 10%, 20%, 30%, and 40% strain were all below 3%, with fluctuations of 1.09%, 1.83%, 2.97%, and 2.22%, respectively. When the strain is 50%, the sensor response fluctuation rises to 6.38% in 5 cycles. Therefore, ANGAs have excellent sensing stability in the strain range of 2% to 40%. It can be observed from Fig. 4e that the average sensor response at 2%, 3%, 5%, 10%, 20%, 30% and 40% are 3.29%, 4.34%, 6.4%, 9.3%, 24.5%, 38.4% and 53.3%, respectively. In order to establish the relationship between the sensor response and the loading pressure, the pressure values at different strains were identified according to Fig. 3a. As can be observed in Fig. 4f, the variation of resistance increases with increasing pressure and the corresponding pressure value (0.044–0.92 kPa) subjected to the sensor can be determined by resistance change from the curve. The detection pressure of ANGAs at 2% strain is 0.044 kPa, which is also the pressure sensing sensitivity of ANGAs. Notably, the upper pressure detection limit increased dramatically by up to 6 times from 0.14 kPa for GAs to 0.92 kPa for ANGAs after coupling with Al_2O_3 nanorods. Considering the relatively large fluctuations at 50% strain, the cyclic durability of the ANGAs was further tested at 40% strain. Thanks to the excellent structural stability of the aerogels, no significant resistance decay was observed in the 500 cycles. In addition, the response fluctuation of ANGAs in 500 cycles is 4.43%, which is slightly higher compared to the fluctuation in 5 cycles (2.22%), but still at a relatively low level. All of the above results indicate that ANGAs can be used as reliable pressure sensors in practical applications.

3.4. Thermal insulation performance of ANGAs

Even though nanorods can form a nanoporous structure that is more conducive to thermal insulation than fibrous aerogels, the ANAs still lead to a rapid increase in thermal conductivity at high temperatures.[39] In addition, for the ordered laminar structured Al_2O_3 nanorod aerogels obtained by directional freeze-drying, gas molecules can still pass through the nanopores between the nanorods for heat transfer between the lamellae. Therefore, the thermal insulation properties of Al_2O_3 nanorod aerogels still need to be further improved.

Generally speaking, for porous materials with pore size less than 1 mm, the total thermal conductivity is considered to be the integrated effect of solid thermal conductivity (λ_s), gas thermal conductivity (λ_g) and radiative thermal conductivity (λ_r).[40] At room temperature, λ_r can usually be neglected due to the small contribution, *i.e.*, the thermal conductivity of the material can be simplified to the sum of λ_s and λ_g.[15] The density and room temperature thermal conductivity of GAs, ANAs, and ANGAs are shown in Fig. 5a and b. The density of the aerogels increases from 1.75 mg cm^{-3} for GAs, 3.13 mg cm^{-3} for ANGA-2 to 8.26 mg cm^{-3} for ANGA-10 as the proportion of nanorods increases. The thermal conductivity of the samples follows the same trend as the density, increasing from 0.0192 W m^{-1} K^{-1} for GAs, 0.0196 W m^{-1} K^{-1} for ANGA-2 to 0.0213 W m^{-1} K^{-1} for ANGA-10, which is due to the growth of λ_s caused by the higher density. However, the thermal conductivity of ANAs (0.0265 W m^{-1} K^{-1}) is still 24.4% higher than that of ANGA-10, even though ANAs have a lower density (7.21 mg cm^{-3}). For ANAs, the overlapped Al_2O_3 nanorods form a porous skeleton (Fig. S4†), so that gas molecules can pass through the pores for heat transfer. For ANGAs, the layered graphene sheets can fill the pores between the nanorods, confining the movement of gas molecules within the gaps of the lamellas. Consequently, the heat transfer through the cell wall is substantially suppressed, which substantially reduces the λ_g. Besides, the ultralow density and narrow bridging between the layers also reduce the λ_s. Therefore, the extremely low λ_s and λ_g together contribute to the super-insulation performance of ANGAs, which even possess a lower thermal conductivity than that of air (0.024 W m^{-1} K^{-1}).[41]

Compared with the polymer reinforced phase, ceramic reinforced graphene aerogel can be used for high-temperature insulation due to its excellent thermostability, so the high-temperature insulation properties of ANGAs have been further investigated (Fig. 5c and d). As predicted, the high-temperature thermal conductivity of ANGAs was dramatically reduced after the incorporation of graphene compared to ANAs, and the difference becomes more pronounced with increasing temperature. At 1000 °C, the thermal conductivity decreased by 26.4% from 0.0988 W m^{-1} K^{-1} for ANAs to 0.0727 W m^{-1} K^{-1} for ANGA-10. According to classical heat transfer theory, λ_r can be represented as:[42]

$$\lambda_r = \frac{16\sigma n^2 T^3}{3\rho e}$$

where σ denotes the Boltzmann constant and n (reflection coefficient) is about 1 for low density aerogels. T, ρ and e represent the temperature, density and specific extinction coefficient of the material, respectively. From the equation, it can be seen that the radiative heat transfer is proportional to T^3, and becomes the dominant heat transfer mode at high temperatures. Al_2O_3 is highly transparent to infrared radiation,[39] while graphene with high specific extinction coefficient can effectively suppress λ_r and thus reduce the total thermal conductivity at high temperatures.[43] It is noteworthy that the thermal conductivity of ANGAs at 1000 °C decreases and then increases with the addition of nanorods, reaching a minimum value of 0.0702 W m^{-1} K^{-1} at ANGA-6, which is the result of the competition between λ_r and λ_s.

According to above equation, the increase in density is beneficial to limit the high temperature radiative heat transfer. At Al_2O_3 nanorod content below 6% (ANGA-6), the decrease in λ_r due to the elevated density can compensate for the increase in λ_s, thus leading to a reduction in total thermal conductivity. As the density of aerogel rises further, the increase in λ_s outweighs the decrease in λ_r, resulting in an increase in thermal conductivity instead. Overall, the lamellar ANGAs with high specific extinction

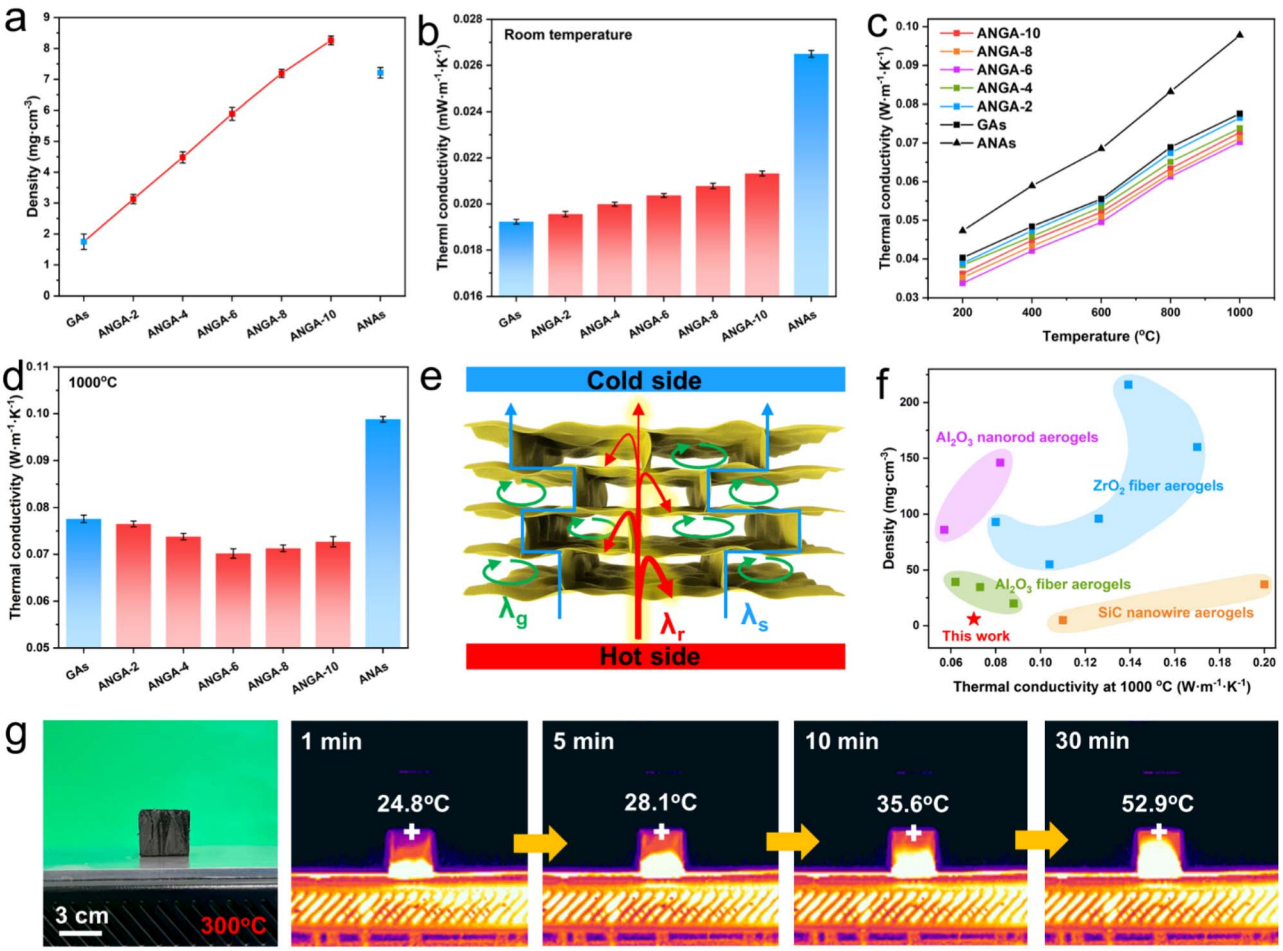

Fig. 5 (a) The density and (b) room temperature thermal conductivity of GAs, ANGAs and ANAs. (c) The high temperature thermal conductivity of curves GAs, ANGAs and ANAs and (d) the corresponding thermal conductivity at 1000 °C. (e) Thermal Superinsulation mechanism diagram of ANGAs. (f) Comparison of density and thermal conductivity at 1000 °C of ANGAs and previously reported ultralight aerogels. (g) Demonstration of thermal insulation performance of ANGAs on a hot plate of 300 °C.

coefficient can significantly weaken the λ_r, and the ultra-low density and the confined lamellar pore structure can effectively suppress the λ_s and λ_g, respectively, so that the ANGAs exhibit superinsulation performance at both high and low temperatures (Fig. 5e). Remarkably, ANGAs show great advantages in density and high-temperature thermal conductivity compared with previously reported ultralight ceramic aerogels (Fig. 5f), including SiC nanowire aerogels (900 °C),[44,45] ZrO_2 fiber aerogels,[14,46–49] Al_2O_3 fiber aerogels[50–52] and Al_2O_3 nanorod aerogels.[15,16] In order to demonstrate the thermal insulation performance of ANGAs more visually, a cube ANGA-6 with a diameter of 3 cm was placed on a heating platform of 300 °C (Fig. 5g). The temperature of the upper surface of the sample increased slowly from 24.8 °C at 1 min, 28.1 °C at 5 min, 35.6 °C at 10 min to 52.9 °C at 30 min, illustrating its great potential as a thermal insulator.

4. Conclusions

In conclusion, high performance ultralight elastic ANGAs were successfully prepared by combining Al_2O_3 nanorods and graphene. This win–win strategy not only overcomes the brittleness of Al_2O_3 nanorod aerogels but also substantially improves the compressive strength of graphene aerogels. The robust backbone enabled the ANGAs to exhibit compressive durability and pressure sensing stability over 500 cycles at 40% strain. In addition, thanks to the graphene with excellent light-shielding capability and the laminar structure obtained by bidirectional freezing, the ANGAs obtained ultra-low thermal conductivity of 0.0196 W m^{-1} K^{-1} and 0.0702 W m^{-1} K^{-1} at 25 °C and 1000 °C, respectively. We believe that this work paves the way for the construction of multifunctional elastic ceramic-based aerogels.

Conflicts of interest

There are no conflicts to declare.

Acknowledgements

The authors thank the financial support from Key R&D Program of Hunan Province (grant number 2022GK2027). All authors contributed to the completion of the manuscript and the final version of the manuscript has been approved by all the authors.

Notes and references

1 X. Xu, S. Fu, J. Guo, H. Li, Y. Huang and X. Duan, *Mater. Today*, 2021, **42**, 162–177.
2 Z. Xiong, Y. Zhu, Z. Wang, Y. Chen and H. Yu, *Adv. Funct. Mater.*, 2021, 2106978.
3 L. Zhu, L. Zong, X. Wu, M. Li, H. Wang, J. You and C. Li, *ACS Nano*, 2018, **12**, 4462–4468.
4 F. Peng, Y. Jiang, J. Feng, H. Cai, J. Feng and L. Li, *Chem. Eng. J.*, 2021, **411**, 128402.
5 F. Peng, Y. Jiang, J. Feng, F. Liu, J. Feng and L. Li, *J. Eur. Ceram. Soc.*, 2022, **42**, 6684–6702.
6 X. Hou, R. Zhang and D. Fang, *Ceram. Int.*, 2017, **43**, 9547–9551.
7 X. Zhang, T. Zhang, Z. Yi, L. Yan, S. Liu, X. Yao, A. Guo, J. Liu and F. Hou, *Ceram. Int.*, 2020, **46**, 28561–28568.
8 H. Maleki, L. Durães and A. Portugal, *Microporous Mesoporous Mater.*, 2014, **197**, 116–129.
9 J. P. Randall, M. A. B. Meador and S. C. Jana, *J. Mater. Chem. A*, 2013, **1**, 6642.
10 Y. Si, X. Wang, L. Dou, J. Yu and B. Ding, *Sci. Adv.*, 2018, **4**, eaas8925.
11 Z. An, C. Ye, R. Zhang and P. Zhou, *Ceram. Int.*, 2019, **45**, 22793–22801.
12 X. Zhang, F. Wang, L. Dou, X. Cheng, Y. Si, J. Yu and B. Ding, *ACS Nano*, 2020, acsnano.0c06423.
13 S. Fu, D. Liu, Y. Deng, J. Guo, H. Zhao, J. Zhou, P. Zhang, H. Yu, S. Dang, J. Zhang, H. Li and X. Xu, *Nano Res.*, 2023, **16**, 5047–5055.
14 J. Guo, S. Fu, Y. Deng, X. Xu, S. Laima, D. Liu, P. Zhang, J. Zhou, H. Zhao, H. Yu, S. Dang, J. Zhang, Y. Zhao, H. Li and X. Duan, *Nature*, 2022, **606**, 909–916.
15 F. Liu, C. He, Y. Jiang, Y. Yang, F. Peng, L. Liu, J. Men, J. Feng, L. Li, G. Tang and J. Feng, *Chem. Eng. J.*, 2023, **455**, 140502.
16 E. Zhang, W. Zhang, T. lv, J. Li, J. Dai, F. Zhang, Y. Zhao, J. Yang, W. Li and H. Zhang, *ACS Appl. Mater. Interfaces*, 2021, **13**, 20548–20558.
17 F. Liu, Y. Jiang, F. Peng, J. Feng, L. Li and J. Feng, *Chem. Eng. J.*, 2023, 141721.
18 X. Xu, Q. Zhang, Y. Yu, W. Chen, H. Hu and H. Li, *Adv. Mater.*, 2016, **28**, 9223–9230.
19 Q. Zhang, X. Xu, D. Lin, W. Chen, G. Xiong, Y. Yu, T. S. Fisher and H. Li, *Adv. Mater.*, 2016, **28**, 2229–2237.
20 F. An, X. Li, P. Min, H. Li, Z. Dai and Z.-Z. Yu, *Carbon*, 2018, **126**, 119–127.
21 Y. Xie, S. Xu, Z. Xu, H. Wu, C. Deng and X. Wang, *Carbon*, 2016, **98**, 381–390.
22 R. Zhang, R. Hu, X. Li, Z. Zhen, Z. Xu, N. Li, L. He and H. Zhu, *Adv. Funct. Mater.*, 2018, **28**, 1705879.
23 Y. Xia, C. Gao and W. Gao, *J. Polym. Sci.*, 2022, **60**, 2239–2261.
24 H. Sun, Z. Xu and C. Gao, *Adv. Mater.*, 2013, **25**, 2554–2560.
25 L. Guan, L. Zhao, Y. Wan and L. Tang, *Nanoscale*, 2018, **10**, 14788–14811.
26 J. Fan, S. Hui, T. P. Bailey, A. Page, C. Uher and F. Yuan, *J. Mater. Chem. A*, 2019, **7**, 1574–1584.
27 Y. Ma, M. Yu, J. Liu, X. Li and S. Li, *ACS Appl. Mater. Interfaces*, 2017, **9**, 27127–27134.
28 H.-L. Gao, Y.-B. Zhu, L.-B. Mao, F.-C. Wang, X.-S. Luo, Y.-Y. Liu, Y. Lu, Z. Pan, J. Ge, W. Shen, Y.-R. Zheng, L. Xu, L.-J. Wang, W.-H. Xu, H.-A. Wu and S.-H. Yu, *Nat. Commun.*, 2016, **7**, 12920.
29 Q. Zhang, F. Zhang, S. P. Madarametla, H. Li, C. Zhou and D. Lin, *Small*, 2016, **12**, 1681–1814.
30 L. Zhou and Z. Xu, *J. Hazard. Mater.*, 2020, **388**, 121804.
31 Q. Zhang, D. Lin, B. Deng, X. Xu, Q. Nian, S. Jin, K. D. Leedy, H. Li and G. J. Cheng, *Adv. Mater.*, 2017, **29**, 1605506.
32 X. Meng, X. Peng, Y. Wei, S. Ramakrishna, Y. Sun and Y. Dai, *Chem. Eng. J.*, 2022, **437**, 135444.
33 H. Yin, S. Zhao, J. Wan, H. Tang, L. Chang, L. He, H. Zhao, Y. Gao and Z. Tang, *Adv. Mater.*, 2013, **25**, 6270–6276.
34 J.-Y. Hong, B. M. Bak, J. J. Wie, J. Kong and H. S. Park, *Adv. Funct. Mater.*, 2015, **25**, 1053–1062.
35 S. Ye, Y. Liu and J. Feng, *ACS Appl. Mater. Interfaces*, 2017, **9**, 22456–22464.
36 F. Peng, Y. Jiang, J. Feng, J. Feng and L. Li, *J. Am. Ceram. Soc.*, 2022, **105**, 2288–2299.
37 J. Shen, Y. Hu, M. Shi, X. Lu, C. Qin, C. Li and M. Ye, *Chem. Mater.*, 2009, **21**, 3514–3520.
38 F. Farivar, P. L. Yap, K. Hassan, T. T. Tung, D. N. H. Tran, A. J. Pollard and D. Losic, *Carbon*, 2021, **179**, 505–513.
39 W. Zou, X. Wang, Y. Wu, L. Zou, G. Zu, D. Chen and J. Shen, *Ceram. Int.*, 2019, **45**, 644–650.
40 L. W. Hrubesh and R. W. Pekala, *J. Mater. Res.*, 1994, **9**, 731–738.
41 X. Zhang, X. Cheng, Y. Si, J. Yu and B. Ding, *ACS Nano*, 2022, **16**, 5487–5495.
42 T. Xie, Y.-L. He and Z.-J. Hu, *Int. J. Heat Mass Transfer*, 2013, **58**, 540–552.
43 G. H. Tang, Y. Zhao and J. F. Guo, *Int. J. Heat Mass Transfer*, 2016, **99**, 192–200.
44 L. Su, H. Wang, M. Niu, X. Fan, M. Ma, Z. Shi and S.-W. Guo, *ACS Nano*, 2018, **12**, 3103–3111.
45 B. Li, X. Yuan, Y. Gao, Y. Wang, J. Liao, Z. Rao, B. Mao and H. Huang, *Mater. Res. Express*, 2019, **6**, 045030.
46 X. Zhang, B. Wang, N. Wu, C. Han, C. Wu and Y. Wang, *J. Eur. Ceram. Soc.*, 2020, **40**, 1877–1885.
47 G. Zu, J. Shen, W. Wang, L. Zou, Y. Lian, Z. Zhang, B. Liu and F. Zhang, *Chem. Mater.*, 2014, **26**, 5761–5772.
48 T. Wang, Q. Yu and J. Kong, *Int. J. Appl. Ceram. Technol.*, 2018, **15**, 472–478.
49 T. Wang, Q. Yu, J. Kong and C. Wong, *Ceram. Int.*, 2017, **43**, 9296–9302.
50 R. Liu, X. Dong, S. Xie, T. Jia, Y. Xue, J. Liu, W. Jing and A. Guo, *Chem. Eng. J.*, 2019, **360**, 464–472.
51 L. Li, C. Jia, Y. Liu, B. Fang, W. Zhu, X. Li, L. Schaefer, Z. Li, F. Zhang, X. Feng, N. Hussain, X. Xi, D. Wang, Y. Lin, X. Wei and H. Wu, *Mater. Today*, 2022, **54**, 72–82.
52 B. Zhang, Y. Liu, Q. Wu, M. Zhou, D. Su, H. Ji and X. Li, *J. Eur. Ceram. Soc.*, 2022, **42**, 5995–6004.